CHEMISTRY OF MATERIALS

# Preferred Site Occupation of Doping Cation and Its Impact on the Local Structure of $V_2O_5$

Qiang Fu,* Anna-Lena Hansen, Björn Schwarz, Angelina Sarapulova, Lihua Zhu, Guiying Tian, Martin Etter, Alexander Missyul, Edmund Welter, Vadim Murzin, Sylvio Indris, Raheleh Azmi, Michael Knapp, Sonia Dsoke, and Helmut Ehrenberg

**Cite This:** *Chem. Mater.* 2022, 34, 9844−9853

Read Online

ACCESS | Metrics & More | Article Recommendations | Supporting Information

**ABSTRACT:** Cation doping is an effective method to alter the local structure and electronic state of $V_2O_5$. While it remains a great challenge to experimentally understand whether the doping cations prefer to replace the V ions or reside between the $V_2O_5$ layers, namely, substitutional or interstitial positions. In this work, cation-doped $V_2O_5$ with different elements M (M = Mn, Ni, and Fe) were synthesized via a hydrothermal method since V and M ions can uniformly distribute in the solution to obtain a homogeneous target material. The impact of doping cations on the local structure of $V_2O_5$ is revealed. Multitechniques demonstrate the existence of a small portion of $V^{4+}$ in the doped samples resulting from the electronic structure change of V. Although the results do not directly certify where the doping cations lie in the $V_2O_5$ structure, all information together provide a hint that the doping cations may prefer to reside on the interstitial positions rather than the substitutional positions.

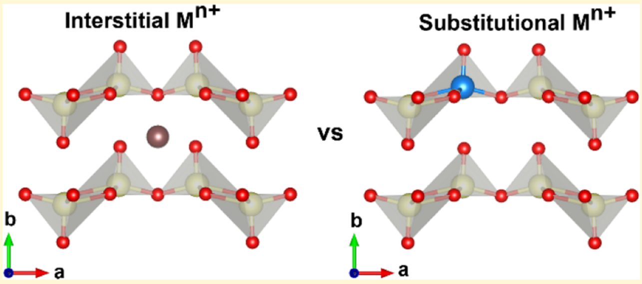

## 1. INTRODUCTION

Vanadium pentoxide ($V_2O_5$) has received intensive application in catalysis, sensors, electrochromic devices, and electrochemistry and as a host material for reversible $Li^+$/$Na^+$ (de)insertion because of its layered structure.[1,2] Cation doping is an effective method to modify the structure and electronic state of electrode materials. In the past decades, a lot of work focused on the doping of $V_2O_5$ nanostructures with various elements to overcome the capacity fading and improve the rate capability in Li-ion batteries (LIBs) and Na-ion batteries (NIBs).[3,4] The doping can increase the electronic conductivity, stabilize the crystal structure of $V_2O_5$ during cycling, and facilitate the charge transfer.[3,4] However, an excess of dopant may block the pathway and reduce the usage of active materials, thus negatively affecting the capacity. In addition, impurities or second phases might be induced by an excess of doping cations, which might, in turn, harm the electrochemical performance of materials. Although cation doping is proven to be an effective approach to improve the electrochemical performance of LIBs and NIBs, it remains a significant challenge to fully understand whether the doping cation prefers to locate the substitutional or interstitial positions and the impact of doping cation on the local structure of $V_2O_5$. Note that substitutional and interstitial doping means that the doped element either replaces the V ions or resides between the $V_2O_5$ layers, respectively.

*Since in the case of doping (especially for semiconductors), the degree of the doping level is well below 0.1%, doping has no significant influence on the (nonlocal) underlying structure. To use the term "doping" is quite common for battery materials research even if the dopant concentrations are high and cause structural modifications. One should note that "doping" is not accurate or appropriate enough to describe such cases. However, it is a great challenge concerning the specific "wording" like this, and "doping" is still used in this manuscript.*

So far, it is unknown whether the preferred site occupation of doping cation and the effects of doping cation on the change of local structure depends on the synthesis route or is associated with the nature of doping cation or maybe both. As demonstrated in previous works, the doping cations, for example, $Zn^{2+}$ [5,6] and $Cu^{2+}$ [5,6] in $V_2O_5$ aerogel/xerogel, $Cr^{3+}$ [7] and $Fe^{3+}$ [8] in crystalline $V_2O_5$, locate in the interlayer spacing/residing between the $V_2O_5$ layers. In these works, a preprepared $V_2O_5$ hydrogel ($V_2O_5{\cdot}nH_2O$) was used as a starting material to obtain the doped material, followed by mixing with a stoichiometric amount of Zn or Cu powder,

Received: June 7, 2022
Revised: October 12, 2022
Published: November 2, 2022

https://doi.org/10.1021/acs.chemmater.2c01695
*Chem. Mater.* 2022, 34, 9844−9853

$Cr(NO_3)_3$ or $FeCl_3$ solution, with or without following heat treatment. However, all of the doping cations would be expected as interstitial doping in these cases since no uniform solution was used. Our aim is to properly study the preferred site occupation of doping cation by applying a uniform solution during synthesis. For this purpose, materials in this study were synthesized through a hydrothermal method enabling cation doping with M (M = Mn, Ni, and Fe) into $V_2O_5$.[9] This way, all of the starting materials were dissolved into an aqueous solution, in which the V and M ions can uniformly distribute in the precursor material to obtain a homogeneous target material after heat treating the precursor.

To gain a complete understanding of preferred site occupations and doping cations on the local structure of $V_2O_5$, several advanced techniques are used including chemical analysis, synchrotron radiation powder diffraction, pair distribution function analysis (PDF), Raman spectroscopy, X-ray photoelectron spectroscopy (XPS), $^{51}V$ nuclear magnetic resonance (NMR) spectroscopy, magnetic measurements, and X-ray absorption spectroscopy (XAS).

## 2. EXPERIMENTAL SECTION

**2.1. Synthesis of M-Doped $V_2O_5$ Materials.** Pristine and M-doped $V_2O_5$ (M = Mn, Ni, and Fe; target M/V = 5% and 10%) were synthesized *via* a hydrothermal method. $MnCl_2$, $NiCl_2$, and $Fe(NO_3)_3$ were used as starting materials to provide the corresponding amount of Mn, Ni, and Fe. Typically, 1.0 mL of 2 M HCl, ammonium metavanadate ($NH_4VO_3$, 0.3 g for pristine $V_2O_5$) with a molar ratio of M/V = 5 and 10%, and 0.5 g of surfactant P123 ($EO_{20}PO_{70}EO_{20}$, where EO and PO represent ethylene oxide and propylene oxide, respectively) were mixed into 30 mL of deionized water under ultrasonication for 10 min and a consequent stirring for 1 h. After that, the mixed solution was transferred to 50 mL Teflon-lined autoclaves and maintained at 120 °C for 24 h with intermittent stirring in an oven. The resulting precipitates were filtered and washed with distilled water and acetone several times, and then dried under vacuum at 120 °C for 24 h. The final products were obtained by annealing at 400 °C for 2 h in air with a heating rate of 10 °C/min.

**2.2. Morphological, Structural, and Surface Characterization.** The morphology was studied with a Zeiss Supra 55 scanning electron microscope (SEM) with primary energy of 15 keV. The structural characterization was performed using synchrotron radiation ($\lambda$ = 0.4132 Å, 30 keV) at the Material Science and Powder Diffraction beamline (MSPD) at ALBA synchrotron (Barcelona, Spain).[10] The diffraction pattern was collected in a capillary by powder filled in a 0.7 mm Ø borosilicate capillary. The synchrotron diffraction data were analyzed by the Rietveld method using the Fullprof software package.[11] The crystallographic model was chosen from Shklover and Haibach's work[12] for the Rietveld refinement of doped samples.

**2.3. Pair Distribution Function Analysis.** X-ray total scattering data, suitable for PDF analysis, were obtained using synchrotron radiation ($\lambda$ = 0.2072 Å, 60 keV) at beamline P02.1, PETRA III, DESY, Hamburg.[13] The powder material was filled in a 0.7 mm Ø borosilicate capillary for PDF measurements, and an empty capillary of borosilicate type was measured for background corrections. A $LaB_6$ standard material (NIST SRM 660b) was measured under similar conditions to get the instrumental resolution ($Q_{damp}$ = 0.018 Å$^{-1}$). The measurements were carried out with a fast area detector from PerkinElmer to collect 2D diffraction images, and then the data were converted into one-dimensional total scattering data with DAWN Science software.[14] The data were corrected for background scattering, Compton scattering, and detector effects. Data were Fourier transformed to $Q_{max}$ = 19.7 Å$^{-1}$ to obtain the PDF $G(r)$ within PDFgetX3.[15] Structure models were refined against the PDF data within PDFgui.[16]

**2.4. X-ray Photoelectron Spectroscopy.** XPS was performed using a K-Alpha$^+$ instrument (Thermo Fisher Scientific) with a monochromatic Al-K$\alpha$ X-ray source (1486.6 eV) with 400 $\mu$m spot size. The sample storage and transportation to the spectrometer for XPS characterization were carried out in an airtight transport vessel under Ar. Thermo Avantage software was used to perform data acquisition and processing as described elsewhere.[17] The spectra were fitted with one or more Voigt profiles. All spectra were referenced to the C 1s peak of adventitious hydrocarbons at 285.0 eV. The analyzer transmission function, Scofield's sensitivity factors,[18] and effective attenuation lengths (EALs) for photoelectrons were applied for quantification, and EALs were calculated using the standard TPP-2M formalism.[19]

**2.5. Raman Measurements.** Raman measurements were carried out with a LabRam Evolution HR from Horiba equipped with Nd:YAG laser (633 nm, 100 mW) and a CCD detector (Horiba). To collect the Raman spectra of all samples, a 600 grating was used to split the measurement signal with a ×100 objective (NA 0.95), and the data collection was conducted for 30 seconds with a laser source of 1 mW.

**2.6. $^{51}V$ Magic-Angle Spinning Nuclear Magnetic Resonance.** $^{51}V$ MAS NMR spectroscopy was performed with a Bruker Avance 200 MHz spectrometer at a magnetic field of 4.7 T, corresponding to a Larmor frequency of 52.6 MHz. Spinning was performed with 1.3 mm zirconia MAS rotors at 55 kHz. The spectra were acquired with a Hahn-echo pulse sequence, a $\pi/2$ pulse length of 1.5 $\mu$s, and a recycle delay of 5 s. The chemical shift of $^{51}V$ was referenced to $VOCl_3$.

**2.7. Ex Situ XAS Measurements.** Ex situ XAS measurements were performed at synchrotron beamlines P64 and P65 at PETRA III (DESY), Hamburg. XAS spectra of vanadium were recorded in quick-XAS (6 min/spectrum) mode in fluorescence geometry using a PIPS (passivated implanted planar silicon) diode. The V, Mn, Ni, and Fe K-edge for doped $V_2O_5$ were measured, and the energy was calibrated utilizing a corresponding foil V, Mn, Ni, and Fe as commonly applied in XAS experiments. $V_2O_3$, $VO_2$, $V_2O_5$, MnO, $Mn_2O_3$, $MnO_2$, NiO, FeO, $Fe_3O_4$, and $Fe_2O_3$ were used as standard materials, respectively. All of the data were collected at room temperature with a Si(111) double-crystal monochromator, and all of the XAS spectra were processed using the DEMETER software package.[20]

**2.8. Magnetic Properties.** Magnetic properties were measured using the vibrating sample magnetometry (VSM) option installed onto a DynaCool Physical Property Measurement System (PPMS) from Quantum Design. Magnetic moment field vs temperature was measured in zero-field cooled (ZFC) and field cooled (FC) mode at a magnetic field of 5 kOe from 2 to 300 K with a temperature resolution of $\Delta T$ = 1 K. Temperature settle mode was used from 2 to 50 K and temperature sweep mode (2 K/min) from 50 to 300 K. Since the ZFC and FC curves coincide over the complete temperature region, only the FC curves are shown in this work. A sample holder "touchdown" was performed every 20 K for precise maintenance of the sample centering (causing some artifacts at high temperatures with low total magnetic moment). The relatively high magnetic field for the temperature scans was chosen to maximize the total measured magnetic moment from samples that exhibit a very low total magnetic moment. Magnetic moment vs field was measured at 2 K from 0 to 70 kOe ($\mu_0 H$ = 7 Tesla). The measured raw data were corrected for diamagnetic contributions from the sample holder ($\chi^{dia}_{holder} = -2.5 \times 10^{-8}$ cm$^3$/holder) and for diamagnetic contribution from the $V^{2+}$ and $O^{2-}$ ions by the incremental method[21] to $\chi^{dia}_{V_2O_5} = -1.59 \times 10^{-5}$ cm$^3$ mol$^{-1}$. Fe-doped samples were not considered for evaluation due to their multiphase nature.

## 3. RESULTS AND DISCUSSION

**3.1. Chemical Analysis.** The doped samples were analyzed by using inductively coupled plasma optical emission spectroscopy (ICP-OES)[22] to determine the content of doped element M in the doped $V_2O_5$ materials. Table 1 provides the determined M/V molar ratio from ICP and estimated

**Table 1. Determined M/V Molar Ratio from ICP, Estimated Stoichiometry for M-Doped $V_2O_5$ (M = Mn, Ni, and Fe), and Their Short Names**

| sample | M/V molar ratio determined (%) | stoichiometry | short name |
|---|---|---|---|
| Mn/V = 5% | 0.5 | $Mn_{0.01}V_2O_5$ | Mn01 |
| Mn/V = 10% | 0.8 | $Mn_{0.016}V_2O_5$ | Mn02 |
| Ni/V = 5% | 0.6 | $Ni_{0.012}V_2O_5$ | Ni01 |
| Ni/V = 10% | 1.1 | $Ni_{0.023}V_2O_5$ | Ni02 |
| Fe/V = 5% | 5.5 | $Fe_{0.11}V_2O_5$ | Fe01 |
| Fe/V = 10% | 11.9 | $Fe_{0.24}V_2O_5$ | Fe02 |

stoichiometry for M-doped $V_2O_5$ (M = Mn, Ni, and Fe; target M/V = 5 and 10%) samples. Therefore, the chemical formula for doped samples is estimated as $Mn_{0.01}V_2O_5$, $Mn_{0.016}V_2O_5$, $Ni_{0.012}V_2O_5$, $Ni_{0.023}V_2O_5$, $Fe_{0.11}V_2O_5$, and $Fe_{0.24}V_2O_5$ according to ICP results. To easily describe the samples, short names are shown in Table 1 for M-doped $V_2O_5$. Note that the atomic ratio of Mn/V and Ni/V is far from the desired value owing to the loss during the hydrothermal synthesis, where only a small amount of Ni and Mn dopes inside the structure and most of the metal remain in the solution and is washed away.

**3.2. Morphological and Structural Characterization.** The crystal structure of the pristine and doped $V_2O_5$ was investigated by synchrotron radiation diffraction, as displayed in Figure S1. The narrow reflections with strong intensities reveal the high crystallinity of all obtained materials. For the pristine $V_2O_5$, Mn01, Mn02, Ni01, and Ni02 (Figure S1a−e), all reflections could be indexed according to the non-centrosymmetric orthorhombic $V_2O_5$ with space group $Pmn2_1$,[12,23] while some additional reflections are obtained for Fe01 and Fe02, in addition to the main phase of orthorhombic $V_2O_5$. The additional reflections belong to a minor amount of monoclinic $Fe_2V_4O_{13}$ phase with a space group of $P21/c$, whose amount is 1 and 5 wt % for Fe01 and Fe02, respectively. The synthesis of Fe-doped samples is quite close to that of $Fe_2V_4O_{13}$ as reported in the literature, which may lead to the formation of impurity $Fe_2V_4O_{13}$.[24] Table S1 displays the starting atomic coordinates of the structural model $(M_xV_2O_5)$[12] for Rietveld refinement. M1 and M2 represent the substitution of V sites (M1) and the interstitial position between the layers (M2) for the doped element M, respectively. The lattice parameters are listed in Table S2 after Rietveld refinement. The pristine $V_2O_5$ has $a$ = 11.5084 (1) Å, $b$ = 4.3739 (1) Å, and $c$ = 3.5640 (1) Å, which are close to those values given in the previous work.[12] However, the large volume difference between both pristine $V_2O_5$ materials synthesized in this work and Shklover's work[12] could be attributed to the significant difference between the two synthesis methods, where it requires a high temperature to melt $V_2O_5$ during the single crystal growth. The lattice

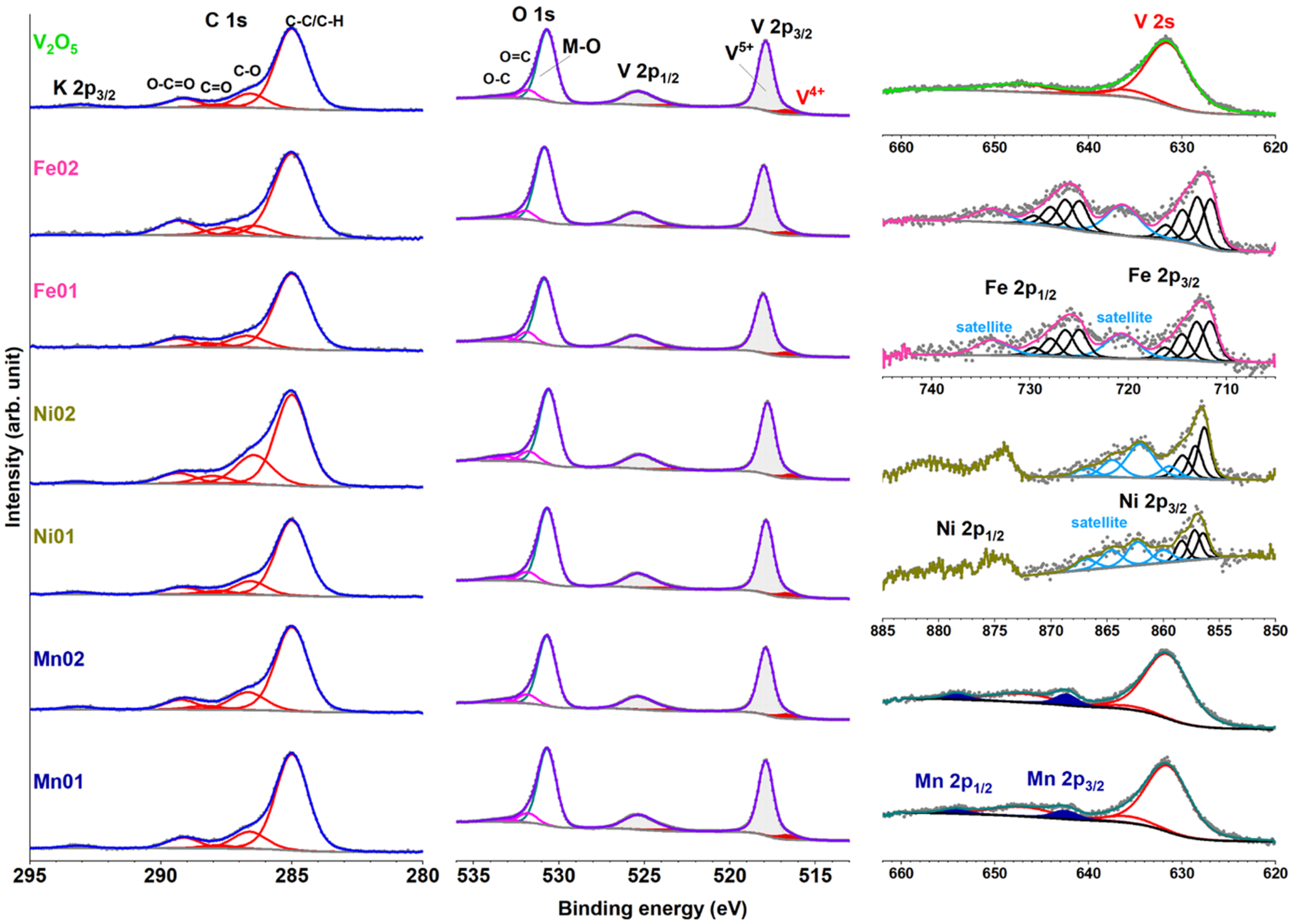

**Figure 1.** C 1s (left column), V 2p and O 1s (middle column), and V 2s, Mn, Ni, and Fe 2p (right column) X-ray photoelectron spectra of pristine and doped materials.

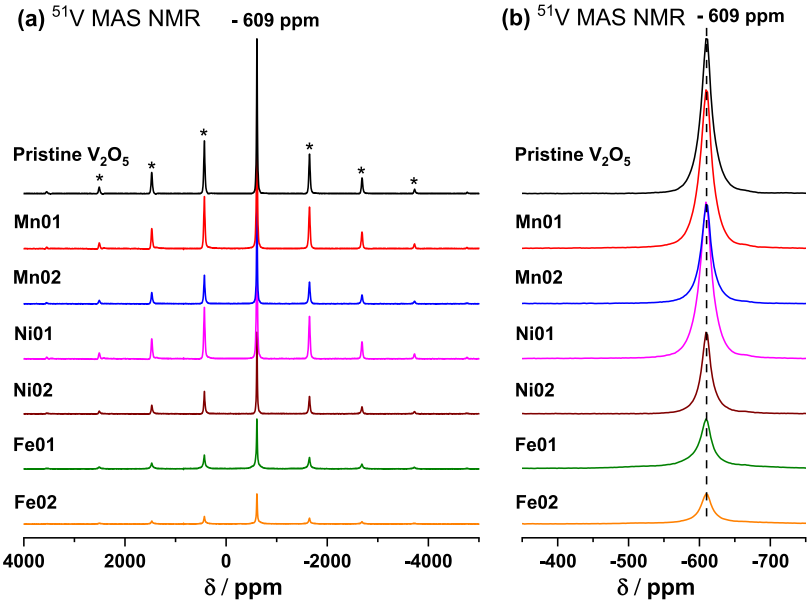

**Figure 2.** $^{51}$V MAS NMR spectra of pristine and doped materials.

parameter *c* remains almost unaffected by the doping. The lattice parameter *a* shows a slight decrease in both Mn-doped samples, while *a* shows a slight increase in Ni-doped samples compared with the pristine one. The lattice parameter *b* for all Mn- and Ni-doped samples first slightly decreases and then increases along with the increasing content of doping cation, compared with that of the pristine one. For Fe-doped samples, the lattice parameters *a* and *b* show larger changes with the continuous increase of *a* and decrease of *b*. The different behaviors of lattice parameters for different samples are related to the radius/oxidation state and the amount of doping cation in each sample, as well as different amounts of $V^{4+}$ in the structure caused by doping. The significant changes in lattice parameters for Fe-doped samples may suggest that the doping amount of Fe inside the structure is larger than that of Ni- and Mn-doped ones. Moreover, magnetic measurements (in later discussion) show the diamagnetic nature of pristine $V_2O_5$, confirming the $V^{5+}$ of the overall pristine sample. Negative occupancies for the M1 sites are observed for all doped samples after the Rietveld refinement. On the other hand, Rietveld refinement confirms the positive occupancies of interstitial sites for M-doped $V_2O_5$. The results indicate that there is a higher possibility for dopants to lie on the interstitial position than that on the substitutional position. As displayed in Figure S2, SEM demonstrates that two Ni-doped samples are composed of both nanowires and nanoparticles, while all of the other samples consist of nanoparticles.

To further study the effect of doping cations on the local structure of $V_2O_5$, Raman spectra were collected for pristine and doped materials, as displayed in Figure S3. Pristine $V_2O_5$ exhibits typical Raman bands as reported in the previous work.[25] Compared with the pristine $V_2O_5$, the Raman spectra of all doped materials do not show a significant shift of the main peak of $V_2O_5$. Two additional bands at 651 and 867 $cm^{-1}$ are observed, and the intensities increase along with the increase in the doping Mn amount. Several additional bands between 750 and 1200 $cm^{-1}$ are also obtained for Fe-doped samples; some of them might be attributed to the impurity $Fe_2V_4O_{13}$. Interestingly, no clear difference is observed for the two Ni-doped samples.

X-ray photoelectron spectroscopy (XPS) was used to investigate the surface chemistry and surface elemental composition of pristine $V_2O_5$ and doped $V_2O_5$ materials, which gives information of around top 10 nm of the surface (according to the applied X-ray energy 1486.6 eV). According to Figure 1 (left column), the C 1s spectrum of all samples can be fitted with 4 peaks at 285.0, 286.5, 288.0, and 289.3 eV, which are ascribed to the C—C/C—H, C—O, C═O, and O—C═O groups, respectively. O—C, O═C could be attributed to the residual surfactant symmetric triblock copolymer P123, which consists of poly(ethylene oxide) (PEO) and poly(propylene oxide) (PPO) and was present during synthesis. There is also residual potassium to be detected on the surface at around 293.2 eV for K $2p_{3/2}$. The V 2p spectrum of all samples (Figure 1, middle column) can be fitted with two doublets: a main one with V $2p_{3/2}$ at around 517.9 eV and a second one with weak intensity at around 516.7 eV,[26] which indicates that V exists mainly in the oxidation state +5 with a minor contribution of vanadium in the +4 state with very similar ratios of $V^{5+}/(V^{4+} + V^{5+})$ (93.4, 93.8, 93.1, 93.6, 94.9, 94, and 93.1%, for pristine, Mn01, Mn02, Ni01, Ni02, Fe01, and Fe02 samples, respectively). The minor $V^{4+}$ on the surface of pristine $V_2O_5$ could be assigned to the reduction of residual surfactant P123 during the annealing at 400 °C. It implies that the oxidation state of V is only slightly influenced by the cations doping when considering the residual surfactant P123 having the same effects for all samples. The O 1s spectrum of pristine $V_2O_5$ can be fitted with three peaks at 533.1, 531.8, and 530.7 eV, which correspond to the O—C, O═C, and V—O groups.[27−29] In contrast, it is very difficult to get the oxidation state of the dopant M (a clear analysis needs multiplet fitting[30]) because of the low intensity of Ni 2p, Fe 2p, and Mn 2p. In the case of Mn-doped samples, an extra dimension of complexity hinders the oxidation state analysis, namely, the overlapping of the Mn 2p spectrum with V 2s (as well as Mn 3s with V 3s and Mn 3p with V 3p) (Figure 1, right column). However, the approximate peak barycenter of Fe 2p at around 711.5 eV and a weak satellite at around 720.5 eV can give a hit on the $Fe^{3+}$ state.

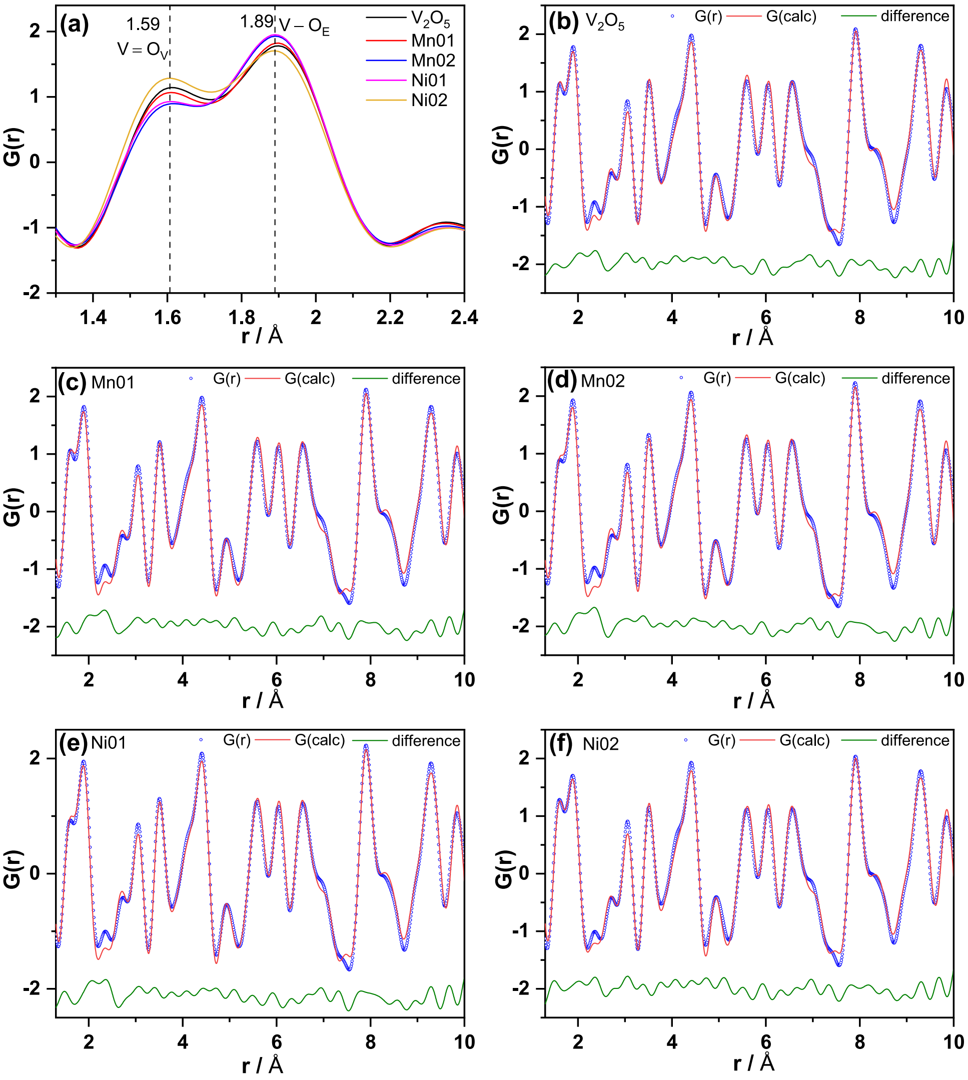

**Figure 3.** Zoom into the (a) PDFs and PDF fitting of (b) pristine $V_2O_5$, (c) Mn01, (d) Mn02, (e) Ni01, and (f) Ni02.

Figure 2 displays the $^{51}$V MAS NMR spectra of pristine and doped materials. The spectrum of pristine $V_2O_5$ exhibits an isotropic shift of −609 ppm, which is attributed to V mainly as diamagnetic $V^{5+}$, being characteristic for $V_2O_5$.[31] Furthermore, this spectrum shows a broad pattern of spinning sidebands reflecting the large nuclear quadrupolar moment of the $^{51}$V nucleus[32] and the asymmetric environment around V in the crystal structure of $V_2O_5$. In this sample, V should be exclusively in the diamagnetic state $V^{5+}$ ($3d^0$). For the samples doped with Mn, Ni, and Fe, the intensity of the spectra is significantly reduced. In all three cases (Mn-, Ni-, Fe-doped), the intensity of the NMR peak is lower for the higher Mn/Ni/Fe concentration. This decrease in intensity is caused by the reduction of $V^{5+}$ to $V^{4+}$ or, in other words, by the stabilization of the $3d^1$ states, i.e., unpaired electron spin density is formed at the V atoms which is causing a strong broadening of the $^{51}$V NMR signal beyond detectability. This is in good agreement with XPS and magnetic results below. This behavior clearly shows that the additional elements (Mn, Ni, or Fe) are incorporated into the crystal structure of $V_2O_5$. The stabilization of the $3d^1$ states will cause the formation of small polarons which in turn will increase the conductivity of the material, but the local distortions can also impede the lithiation of $V_2O_5$.[33] Moreover, the Fe-doped samples show a weak signal at −268 ppm.

PDF analysis is sensitive to the local atomic ordering and is applied to investigate the influence of doping on the structure. Figure S4a compares the PDFs of all samples. No major differences can be observed at first glance regarding the coherence length or intensity of the PDF peaks. This indicates that all samples reveal the same degree of crystallinity as the reference $V_2O_5$ sample (in black). On the other hand, small shifts in Figure S4b are observed compared with reference $V_2O_5$, revealing differences in the global structure owing to different cell parameters as proven by XRD (Table S2).

The local structure, represented by the PDF in Figure S4c, does not show any major alterations as well. The most pronounced changes affect the first peak (Figure 3a), corresponding to the V═O vanadyl bond (1.59 Å). The first two peaks correspond to the V═O vanadyl bond and the V−O equatorial bond (Figure S5), respectively, and coincide well with the expected values given in Table S3. The changes in the V═O and V−O bond lengths caused by cation doping are depicted in Figure S5a,b. Both bond lengths are shortened in the doped samples but with rather small changes, <1%. More obvious changes can be observed for the integrated intensities of both types of bonds, i.e., the vanadyl and the V−O bond

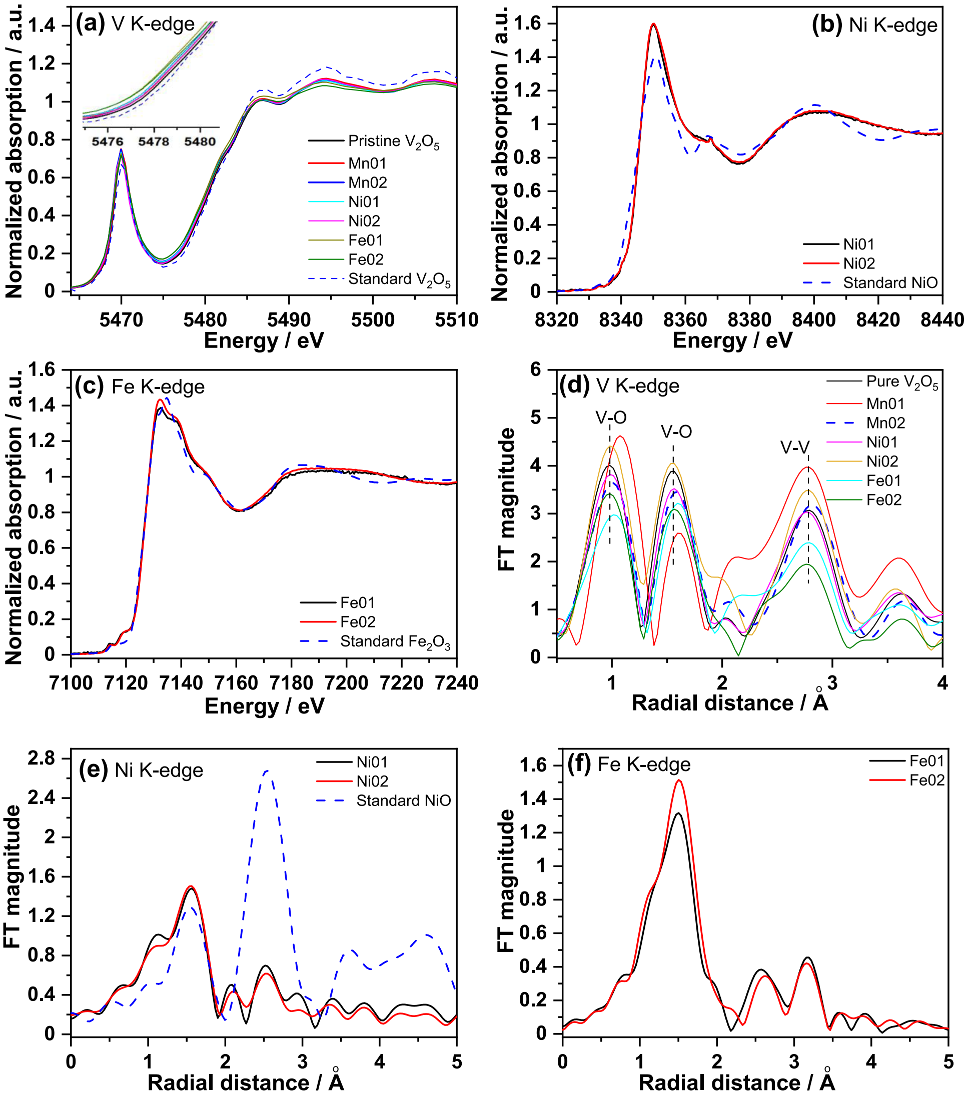

**Figure 4.** XANES spectra and phase-uncorrected Fourier transforms (FT) of (a, d) V K-edge, (b, e) Ni K-edge, and (c, f) Fe K-edge EXAFS ($k^3$-weighted) for pristine and doped materials.

(Figure S5c,d), where the integrated intensities of the PDF peaks correlate to the amount of the respective atom−atom distances. The amount of vanadyl bonds is clearly decreased in the doped samples, while an increased intensity of V−O bonds can be observed, indicating the increased amount of V−O bonds. Note that these bonds represent metal−oxygen (M−O) bonds in general because V, Mn, and Ni cannot be distinguished using X-rays due to their similar electron density. Nevertheless, it is possible to ascribe typical bond lengths in the pair distribution function, for example, the unique bond length of 1.59 Å for the V═O vanadyl bond. Nevertheless, the local structure of $V_2O_5$ is changed by cations doping although interstitial or substitutional doping cannot be concluded by PDF. However, the Ni02 sample shows a different behavior compared to the others, which may suggest that the doping mechanism is different for Ni02. This point needs to be clarified in a further study with the help of other techniques such as neutron-based diffraction/PDF. All PDFs could be fitted using an orthorhombic $V_2O_5$ structure model with the space group *Pmn*$2_1$ (Figure 3b−f). The overall symmetry and all cell parameters are not significantly changed by cations doping. As a result, only minor volume changes are observable, as shown in Figure S6. On the other hand, the values obtained from Rietveld refinement (XRD) stay almost constant at ∼179.4 Å$^3$. It is not uncommon that the absolute values obtained by XRD and PDF analysis differ because different amounts of atoms in the structure are averaged over. Moreover, PDF is a total scattering approach and can detect even minor changes in the structure, which are not accessible by analyzing the Bragg intensity only (XRD). The relative volume change from PDF is not as one would expect it by simply comparing the cation sizes (Figure S7), where $V^{5+}$ has the smallest radius, indicating that Mn and Ni are maybe in a highly oxidized state. Nevertheless, due to the similarity of the doped cations and the observation, that the local structural changes are mainly caused by the different amounts of $V^{4+}$ in the structure, PDF analysis is not able to provide solid evidence about the location of the dopants in the local structure of the doped $V_2O_5$.

To investigate the oxidation states and local electron environment of vanadium and dopants, XAS was performed for the pristine and doped samples. The edge position of the V K-edge in the pristine $V_2O_5$ material is slightly lower than that of standard $V_2O_5$ reference (Figure 4a), indicating that the

https://doi.org/10.1021/acs.chemmater.2c01695
Chem. Mater. 2022, 34, 9844−9853

oxidation state of V in $V_2O_5$ is mainly +5 and in good agreement with the XPS and magnetization results below. Moreover, an intense pre-edge peak for the V K-edge of pristine $V_2O_5$ is observed, which is attributed to the transitions between the 1s and bound p-hybridized d-states[34,35] when the centrosymmetric character of the V site is lost. This may suggest that the noncentrosymmetric setting (space group $Pmn2_1$) is more appropriate in this case compared with the centrosymmetric one (space group *Pmmn*) because the increase in symmetry leads to a decrease in the prepeak intensity owing to the decreased probability of the 1s−3d transition.[23] Interestingly, the edge position of V K-edge in all doped $V_2O_5$ samples is slightly lower than that of pristine $V_2O_5$ (Figure 4a), demonstrating that the average oxidation state of V in doped samples is slightly lower compared with the pristine sample. The edge position of Ni K-edge for both Ni-doped $V_2O_5$ materials overlaps with each other (Figure 4b). Figure 4b,e suggests that the oxidation state of Ni is +2 in both Ni-doped materials. Figure 4c shows that the oxidation state of Fe is +3 for both Fe-doped samples. The two compositions with Ni and Fe doping have a slightly reduced oxidation state of V.

The local structure of V ions was further investigated by analyzing the phase-uncorrected Fourier transform (FT) ($k^3$-weighted) of the V K-edge extended X-ray absorption fine structure (EXAFS). It exhibits two FT peaks at 1.0 and 1.55 Å corresponding to the V−O bonds in distorted $[VO_6]$ octahedra and one FT peak at 2.76 Å assigned to the V−V shell for pristine $V_2O_5$ (Figure 4d).[36−39] After doping, only Ni02 shows an increase in amplitude at both V—O bonds, while Mn01 displays an increase in the amplitude of V═O at 1.0 Å and a decrease in that of V—O at 1.55 Å, which is in good agreement with the PDF results; the rest of the samples show a decrease of both V—O bonds. This indicates that the local structure of V has changed to less distorted $[VO_6]$ octahedra of high symmetry from $[VO_5]$ pyramids in Ni02 and to highly distorted $[VO_6]$ octahedra from $[VO_5]$ pyramids in the other doped samples since the smaller amplitude it has, the more distorted is the octahedron, leading to lower symmetry of V. The different behavior may suggest a different doping mechanism for the Ni02 sample, which needs further study using neutron-based techniques, as pointed out in the PDF part. The introduction of doping ions changes the valence of the vanadium ions and lattice structural distortion, which is evident in the local symmetry of the $VO_6$ octahedra.[39] Fourier transforms (FT) of M (M = Ni and Fe) K-edge EXAFS spectra for all doped compounds (Figure 4e,f) show strong interaction in the M—O shell and low amplitude for the M−M shell.[5] As in the case of the Fe- and Ni-doped samples, the first shell represents the main signal, and the Ni−Ni and Fe−Fe contributions are negligible. The contribution of a two-body M—M interaction is not significant in these samples, which can be due to the doping in the host $V_2O_5$ structure. However, high-quality Mn K-edge spectra for both Mn-doped samples are not available probably because of the very low concentration in the doped samples.

Magnetic properties of pristine and doped $V_2O_5$ were investigated to get information about the electronic configurations of V and M ions and their concentrations. The diamagnetic nature of $V_2O_5$ with $V^{5+}$ in the [Ar] electronic configuration is confirmed by the absent magnetic signal even at a very low temperature (10 K) and high magnetic field (10 kOe). The difference between magnetic and XPS results could be understandable since magnetic measurements are a bulk method and sensitive to $V^{4+}$, while XPS is a surface-sensitive method with information depth of around top 10 nm of the surface. This indicates that the concentration of $V^{4+}$ in the overall pristine sample is precious few. In contrast, the Ni- and Mn-doped samples exhibit Langevin-type paramagnetism caused by localized magnetic moments with the magnetization signal inversely proportional to the temperature (Figure S8). According to expression (1), molar Curie constant $C_{\mathrm{mol}}$, Curie−Weiss constant $\theta$, and temperature-independent contribution $\chi_{\mathrm{TI}}$ were determined for all samples and are summarized in Table 2. The $\chi_{\mathrm{TI}}$-corrected inverse molar susceptibility $\chi_{\mathrm{mol}}^{-1}$ vs temperature curves with exclusively Langevin-type magnetic contributing are plotted in Figure 5a. Note that only the temperature region from 2 to 90 K has been used for the Curie−Weiss fits since the very small total magnetic moments of these doped samples lead to strong artifacts in the inverse susceptibility curves at higher temperatures due to the sample recentering procedures (Figure S9). The Curie−Weiss constants $\theta$ show small negative values, indicating very weak antiferromagnetic mean field interaction and/or weak magnetic anisotropies as also revealed by the low-temperature field scans presented below.

**Table 2. Summary of $C_{\mathrm{mol}}$, $\theta$ and $\chi_{\mathrm{TI}}$ for Mn01, Mn02, Ni01, and Ni02 Samples**

| sample | $C_{\mathrm{mol}} \times 10^3$(cm$^3$ K mol$^{-1}$) | $\theta$ (K) | $\chi_{\mathrm{TI}} \times 10^4$(cm$^3$ mol$^{-1}$) |
|---|---|---|---|
| Mn01 | 40.07(5) | −1.7(1) | 3.631(5) |
| Mn02 | 77.1(2) | −4.1(1) | 3.073(7) |
| Ni01 | 14.72(3) | −3.4(1) | 3.398(6) |
| Ni02 | 30.06(7) | −3.8(1) | 4.357(9) |

$$\chi_{\mathrm{mol}}^{-1} = \left(\frac{C_{\mathrm{mol}}}{T - \theta} + \chi_{\mathrm{TI}}\right)^{-1} \tag{1}$$

The Curie constant depends on the concentration and the size of the quadratic magnetic moments (expression S1). Since the introduction of Ni or Mn as dopants can partially cause reduction of $V^{5+}$ to $V^{4+}$ owing to charge neutrality, magnetic moments stemming from V ions and Ni or Mn ions have to be considered here. For instance, when a $Ni^{2+}$ ion would be inserted into the host lattice, two $V^{5+}$ would be reduced to two $V^{4+}$ to keep charge neutrality, and as a consequence, one $Ni^{2+}$ and two $V^{4+}$ would contribute with their magnetic moments. Three different cases will be considered: (a) $M^{2+}$, (b) $M^{3+}$, or (c) $M^{4+}$ of different hypothetical M ion oxidation states. The overview of all scenarios and the resultant relationship between the atomic concentration of the doped species $\gamma_{\mathrm{M}}$ and the concentration of reduced V ions $\gamma_{V4+}$ are listed in Table S4. As a result, the Curie constant can be expressed as a function of a single atomic concentration species $\gamma_{\mathrm{M}}$ of the doped M ion only (third column Table S4), as outlined in expressions S1−S5, and the corresponding involved magnetic moments are listed in Table S5. Figure 5b shows that all determined atomic concentrations $\gamma_{\mathrm{M}}$ are close to those values as determined by ICP, inherently validating to a certain extent the correctness of our assumptions outlined above. This indicates that the combination of multiple methods can provide consistent and reliable results and suitable interpretation from all aspects. According to the Brillouin function (expressions S6−S8), the qualitative evolution of the magnetic moment with the field at a low temperature specifically depends on the size of the magnetic moment. In this case, magnetic interactions and/or

https://doi.org/10.1021/acs.chemmater.2c01695
*Chem. Mater.* 2022, 34, 9844−9853

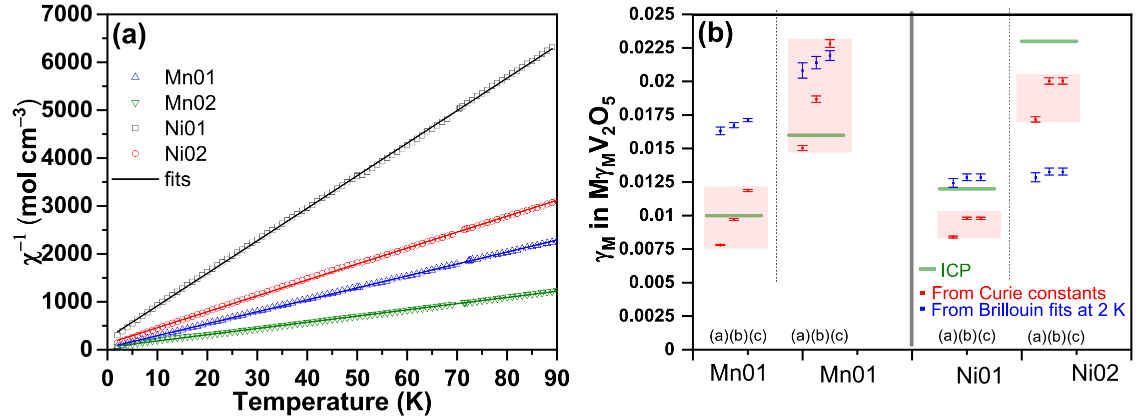

**Figure 5.** (a) Curie−Weiss fitting of the inverse susceptibility data at the range from 2 to 90 K and (b) the atomic concentrations $\gamma_M$ for the Ni- and Mn-doped samples for all scenarios.

crystal anisotropies play a role here, predominantly at very low temperatures as already indicated by the nonvanishing Curie−Weiss constants $\theta$. Consequently, the fits including our boundary conditions (expressions S9 and S10) cannot fully describe the field scans measured at 2 K, i.e., since the magnetization has not saturated even at 7 tesla (Figure S10). The extracted values from the Brillouin fits (Figure 5b) reflect the concentrations $\gamma_M$ to the right order of magnitude. The concentrations determined from Curie constants and Brillouin fits return similar values for the three models. The magnetic moment is stepwise decreasing when the oxidation state of M is increasing, which is partially compensated by the simultaneous increasing number of $V^{4+}$ ions. For instance, the effective paramagnetic moment is stepwise decreasing from 2.82 to 1.73 to 0 $\mu_B$ for $Ni^{2+}$, $Ni^{3+}$, and $Ni^{4+}$, respectively, but this is compensated by the increasing number of $V^{4+}$ ions due to charge neutrality each contributing with 1.73 $\mu_B$.

By considering all results from the individual techniques above, it is still unclear whether the doping cation (M has an oxidation state of 2, 3, or 4) prefers to locate the substitutional or interstitial positions in the $V_2O_5$ host. For the substitutional case, it would lead to a formula of $M_xV_{2-x}O_{5-\delta}$, where oxygen vacancy is introduced to keep charge neutrality. However, in the substitutional doping case, a minor reduction of $V^{5+}$ to $V^{4+}$ cannot be completely excluded and will need more charge compensation by oxygen vacancy in the structure. However, it has a formula $M_xV_2O_5$ for the interstitial case since the cation introduction would result in the reduction of $V^{5+}$ to $V^{4+}$ to keep charge neutrality as frequently reported.[3,40,41] In this work, the existence of a small portion of $V^{4+}$ in the doped samples, which is caused by the electronic structure change of V, is revealed by several techniques including XPS, XAS, NMR, and magnetic measurements in agreement with each other. In addition, positive occupancies of interstitial sites and negative occupancies of substitutional sites together indicate the possible existence of dopants on the interstitial sites of M-doped $V_2O_5$. Taking into account all this information, this work gives a hint that the doping cations may prefer to lie on the interstitial positions rather than the substitutional positions.

## 4. SUMMARY

Pristine and M-doped $V_2O_5$ materials (M = Mn, Ni, and Fe) were synthesized through a hydrothermal method, and the chemical compositions of doped samples are determined by ICP-OES. Pristine and both Mn- and Ni-doped $V_2O_5$ are single-phase, and a small amount of phase impurity $Fe_2V_4O_{13}$ is obtained for Fe-doped samples in addition to the orthorhombic phase $V_2O_5$. The local structural changes caused by the doping cation (substitutional or interstitial doping) in $V_2O_5$ are revealed with three different examples (Mn, Ni, and Fe). Complementary techniques demonstrate the existence of a small portion of $V^{4+}$ in the doped samples resulting from the electronic structure change of V. Although the results do not directly prove whether the doping cations lie in the $V_2O_5$ structure, all information together offer a hint that the doping cations may prefer to reside on the interstitial positions rather than the substitutional positions.

## ■ ASSOCIATED CONTENT

### Supporting Information

The Supporting Information is available free of charge at https://pubs.acs.org/doi/10.1021/acs.chemmater.2c01695.

> Expressions S1−S10 for magnetic parts; Rietveld refinement results of synchrotron diffraction data; SEM images; PDF results; magnetic results; tables for structure model; crystallographic parameters; bond length of M−O; and magnetic results (PDF)

## ■ AUTHOR INFORMATION

### Corresponding Author

**Qiang Fu** − *Institute for Applied Materials (IAM), Karlsruhe Institute of Technology (KIT), D-76344 Eggenstein-Leopoldshafen, Germany;* orcid.org/0000-0002-2507-5477; Phone: 49-721 608-41445; Email: qiang.fu@kit.edu; Fax: 49-721 608-28521

### Authors

**Anna-Lena Hansen** − *Institute for Applied Materials (IAM), Karlsruhe Institute of Technology (KIT), D-76344 Eggenstein-Leopoldshafen, Germany*

**Björn Schwarz** − *Institute for Applied Materials (IAM), Karlsruhe Institute of Technology (KIT), D-76344 Eggenstein-Leopoldshafen, Germany;* orcid.org/0000-0002-9461-1448

**Angelina Sarapulova** − *Institute for Applied Materials (IAM), Karlsruhe Institute of Technology (KIT), D-76344 Eggenstein-Leopoldshafen, Germany;* orcid.org/0000-0003-4643-3912

**Lihua Zhu** − *Institute for Applied Materials (IAM), Karlsruhe Institute of Technology (KIT), D-76344 Eggenstein-Leopoldshafen, Germany*
**Guiying Tian** − *Institute for Applied Materials (IAM), Karlsruhe Institute of Technology (KIT), D-76344 Eggenstein-Leopoldshafen, Germany; College of Chemical Engineering and Materials Science, Tianjin University of Science and Technology, 300457 Tianjin, P. R. China*
**Martin Etter** − *Deutsches Elektronen-Synchrotron DESY, D-22607 Hamburg, Germany*
**Alexander Missyul** − *CELLS-ALBA Synchrotron, E-08290 Cerdanyola del Valles, Barcelona, Spain;* orcid.org/0000-0002-0577-4481
**Edmund Welter** − *Deutsches Elektronen-Synchrotron DESY, D-22607 Hamburg, Germany*
**Vadim Murzin** − *Deutsches Elektronen-Synchrotron DESY, D-22607 Hamburg, Germany;* orcid.org/0000-0003-2743-8398
**Sylvio Indris** − *Institute for Applied Materials (IAM), Karlsruhe Institute of Technology (KIT), D-76344 Eggenstein-Leopoldshafen, Germany;* orcid.org/0000-0002-5100-113X
**Raheleh Azmi** − *Institute for Applied Materials (IAM), Karlsruhe Institute of Technology (KIT), D-76344 Eggenstein-Leopoldshafen, Germany*
**Michael Knapp** − *Institute for Applied Materials (IAM), Karlsruhe Institute of Technology (KIT), D-76344 Eggenstein-Leopoldshafen, Germany;* orcid.org/0000-0003-0091-8463
**Sonia Dsoke** − *Institute for Applied Materials (IAM), Karlsruhe Institute of Technology (KIT), D-76344 Eggenstein-Leopoldshafen, Germany;* orcid.org/0000-0001-9295-2110
**Helmut Ehrenberg** − *Institute for Applied Materials (IAM), Karlsruhe Institute of Technology (KIT), D-76344 Eggenstein-Leopoldshafen, Germany;* orcid.org/0000-0002-5134-7130

Complete contact information is available at:
https://pubs.acs.org/10.1021/acs.chemmater.2c01695

## Notes

The authors declare no competing financial interest.

## ■ ACKNOWLEDGMENTS

This work contributes to the research performed at CELEST (the Center for Electrochemical Energy Storage Ulm-Karlsruhe) and was funded by the German Research Foundation (DFG) under Project ID 390874152 (POLiS Cluster of Excellence). This research work has gained benefit from beamtime allocation (2017092405) at BL04−MSPD at ALBA Synchrotron, Barcelona, Spain. The authors acknowledge DESY (Hamburg, Germany), a member of the Helmholtz Association HGF, for the provision of experimental facilities. Parts of this research were carried out at PETRA III beamlines P02.1, P64, and P65. Beamtime was allocated for proposal(s) I-20160801, 20180707, and I-20190446. The authors would like to thank Nadine Michenfelder for her assistance with material synthesis and Aiswarya Bhaskar for the discussion. Bettina Hunzinger and Thomas Bergfeldt (IAM-AWP) are gratefully acknowledged for SEM and ICP-OES measurements, respectively.

## ■ REFERENCES

(1) Wang, Y.; Cao, G. Synthesis and Enhanced Intercalation Properties of Nanostructured Vanadium Oxides. *Chem. Mater.* **2006**, *18*, 2787−2804.

(2) Sakunthala, A.; Reddy, M. V.; Selvasekarapandian, S.; Chowdari, B. V. R.; Selvin, P. C. Energy storage studies of bare and doped vanadium pentoxide, $(V_{1.95}M_{0.05})O_5$, M = Nb, Ta, for lithium ion batteries. *Energy Environ. Sci.* **2011**, *4*, 1712−1725.

(3) Yao, J.; Li, Y.; Massé, R. C.; Uchaker, E.; Cao, G. Revitalized interest in vanadium pentoxide as cathode material for lithium-ion batteries and beyond. *Energy Storage Mater.* **2018**, *11*, 205−259.

(4) Huang, X.; Rui, X.; Hng, H. H.; Yan, Q. Vanadium Pentoxide-Based Cathode Materials for Lithium-Ion Batteries: Morphology Control, Carbon Hybridization, and Cation Doping. *Part. Part. Syst. Charact.* **2015**, *32*, 276−294.

(5) Frabetti, E.; Deluga, G. A.; Smyrl, W. H.; Giorgetti, M.; Berrettoni, M. X-ray absorption spectroscopy study of $Cu_{0.25}V_2O_5$ and $Zn_{0.25}V_2O_5$ aerogel-like cathodes for lithium batteries. *J. Phys. Chem. B* **2004**, *108*, 3765−3771.

(6) Giorgetti, M.; Berrettoni, M.; Smyrl, W. H. Doped $V_2O_5$-Based Cathode Materials: Where Does the Doping Metal Go? An X-ray Absorption Spectroscopy Study. *Chem. Mater.* **2007**, *19*, 5991−6000.

(7) Soudan, P.; Pereira-Ramos, J. P.; Grégoire, G.; Baffier, N. The sol-gel mixed oxide $Cr_{0.11}V_2O_{5.16}$: An attractive cathodic material for secondary lithium batteries. *Ionics* **1997**, *3*, 261−264.

(8) Maingot, S.; Deniard, P.; Baffier, N.; Pereira-Ramos, J. P.; Kahn-Harari, A.; Brec, R.; Willmann, P. Origin of the improved cycling capability of sol-gel prepared $Fe_{0.12}V_2O_{5.16}$ compared with $V_2O_5$. *J. Power Sources* **1995**, *54*, 342−345.

(9) Darr, J. A.; Zhang, J.; Makwana, N. M.; Weng, X. Continuous Hydrothermal Synthesis of Inorganic Nanoparticles: Applications and Future Directions. *Chem. Rev.* **2017**, *117*, 11125−11238.

(10) Fauth, F.; Peral, I.; Popescu, C.; Knapp, M. The new Material Science Powder Diffraction beamline at ALBA Synchrotron. *Powder Diffr.* **2013**, *28*, S360−S370.

(11) Rodríguez-Carvajal, J. Recent Developments of the Program FULLPROF. *in Commission on Powder Diffraction (IUCr). Newsletter* **2001**, *26*, 12−19.

(12) Shklover, V.; Haibach, T.; Ried, F.; Nesper, R.; Novák, P. Crystal Structure of the Product of $Mg^{2+}$ Insertion into $V_2O_5$ Single Crystals. *J. Solid State Chem.* **1996**, *123*, 317−323.

(13) Dippel, A.-C.; Liermann, H.-P.; Delitz, J. T.; Walter, P.; Schulte-Schrepping, H.; Seeck, O. H.; Franz, H. Beamline P02.1 at PETRA III for high-resolution and high-energy powder diffraction. *J. Synchrotron Radiat.* **2015**, *22*, 675−687.

(14) Filik, J.; Ashton, A. W.; Chang, P. C. Y.; Chater, P. A.; Day, S. J.; Drakopoulos, M.; Gerring, M. W.; Hart, M. L.; Magdysyuk, O. V.; Michalik, S.; et al. Processing two-dimensional X-ray diffraction and small-angle scattering data in DAWN 2. *J. Appl. Crystallogr.* **2017**, *50*, 959−966.

(15) Juhás, P.; Davis, T.; Farrow, C. L.; Billinge, S. J. L. PDFgetX3: a rapid and highly automatable program for processing powder diffraction data into total scattering pair distribution functions. *J. Appl. Crystallogr.* **2013**, *46*, 560−566.

(16) Farrow, C. L.; Juhas, P.; Liu, J. W.; Bryndin, D.; Božin, E. S.; Bloch, J.; Th, P.; Billinge, S. J. L. PDFfit2 and PDFgui: computer programs for studying nanostructure in crystals. *J. Condens. Matter Phys.* **2007**, *19*, No. 335219.

(17) Parry, K. L.; Shard, A. G.; Short, R. D.; White, R. G.; Whittle, J. D.; Wright, A. ARXPS characterisation of plasma polymerised surface chemical gradients. *Surf. Interface Anal.* **2006**, *38*, 1497−1504.

(18) Scofield, J. H. Hartree-Slater subshell photoionization cross-sections at 1254 and 1487 eV. *J. Electron Spectrosc. Relat. Phenom.* **1976**, *8*, 129−137.

(19) Tanuma, S.; Powell, C. J.; Penn, D. R. Calculations of electron inelastic mean free paths. V. Data for 14 organic compounds over the 50−2000 eV range. *Surf. Interface Anal.* **1994**, *21*, 165−176.

(20) Ravel, B.; Newville, M. ATHENA, ARTEMIS, HEPHAESTUS: data analysis for X-ray absorption spectroscopy using IFEFFIT. *J. Synchrotron Radiat.* **2005**, *12*, 537−541.

(21) Lueken, H.Einheiten, Konstanten, Inkremente. In *Magnetochemie: Eine Einführung in Theorie und Anwendung*, Vieweg+Teubner Verlag: Wiesbaden, 1999; pp 421−427.

(22) Kasnatscheew, J.; Evertz, M.; Streipert, B.; Wagner, R.; Klöpsch, R.; Vortmann, B.; Hahn, H.; Nowak, S.; Amereller, M.; Gentschev, A. C.; et al. The truth about the 1st cycle Coulombic efficiency of $LiNi_{1/3}Co_{1/3}Mn_{1/3}O_2$ (NCM) cathodes. *Phys. Chem. Chem. Phys.* **2016**, *18*, 3956−3965.

(23) Fu, Q.; Sarapulova, A.; Zhu, L.; Melinte, G.; Missyul, A.; Welter, E.; Luo, X.; Knapp, M.; Ehrenberg, H.; Dsoke, S. In operando study of orthorhombic $V_2O_5$ as positive electrode materials for K-ion batteries. *J. Energy Chem.* **2021**, *62*, 627−636.

(24) Muthuvel, I.; Gowthami, K.; Thirunarayanan, G.; Suppuraj, P.; Krishnakumar, B.; do Nascimento Sobral, A. J. F.; Swaminathan, M. Graphene oxide−$Fe_2V_4O_{13}$ hybrid material as highly efficient hetero-Fenton catalyst for degradation of methyl orange. *Int. J. Ind. Chem.* **2019**, *10*, 77−87.

(25) Baddour-Hadjean, R.; Pereira-Ramos, J. P.; Navone, C.; Smirnov, M. Raman Microspectrometry Study of Electrochemical Lithium Intercalation into Sputtered Crystalline $V_2O_5$ Thin Films. *Chem. Mater.* **2008**, *20*, 1916−1923.

(26) Silversmit, G.; Depla, D.; Poelman, H.; Marin, G. B.; De Gryse, R. Determination of the V2p XPS binding energies for different vanadium oxidation states ($V^{5+}$ to $V^{0+}$). *J. Electron Spectrosc. Relat. Phenom.* **2004**, *135*, 167−175.

(27) López, G. P.; Castner, D. G.; Ratner, B. D. XPS O 1s binding energies for polymers containing hydroxyl, ether, ketone and ester groups. *Surf. Interface Anal.* **1991**, *17*, 267−272.

(28) Zhu, K.; Qiu, H.; Zhang, Y.; Zhang, D.; Chen, G.; Wei, Y. Synergetic Effects of $Al^{3+}$ Doping and Graphene Modification on the Electrochemical Performance of $V_2O_5$ Cathode Materials. *ChemSusChem* **2015**, *8*, 1017−1025.

(29) Światowska-Mrowiecka, J.; Maurice, V.; Zanna, S.; Klein, L.; Marcus, P. XPS study of Li ion intercalation in $V_2O_5$ thin films prepared by thermal oxidation of vanadium metal. *Electrochim. Acta* **2007**, *52*, 5644−5653.

(30) Azmi, R.; Trouillet, V.; Strafela, M.; Ulrich, S.; Ehrenberg, H.; Bruns, M. Surface analytical approaches to reliably characterize lithium ion battery electrodes. *Surf. Interface Anal.* **2018**, *50*, 43−51.

(31) Gee, B. A.; Wong, A. Vanadium-51 MAS and Static NMR Studies of the Binary $V_2O_5$−$WO_3$ System. *J. Phys. Chem. B* **2003**, *107*, 8382−8387.

(32) Pyykkö, P. Year-2008 nuclear quadrupole moments. *Mol. Phys.* **2008**, *106*, 1965−1974.

(33) De Jesus, L. R.; Horrocks, G. A.; Liang, Y.; Parija, A.; Jaye, C.; Wangoh, L.; Wang, J.; Fischer, D. A.; Piper, L. F. J.; Prendergast, D.; Banerjee, S. Mapping polaronic states and lithiation gradients in individual $V_2O_5$ nanowires. *Nat. Commun.* **2016**, *7*, No. 12022.

(34) Tanaka, T.; Yamashita, H.; Tsuchitani, R.; Funabiki, T.; Yoshida, S. X-ray absorption (EXAFS/XANES) study of supported vanadium oxide catalysts. Structure of surface vanadium oxide species on silica and [gamma]-alumina at a low level of vanadium loading. *J. Chem. Soc., Faraday Trans. 1* **1988**, *84*, 2987−2999.

(35) Wong, J.; Lytle, F. W.; Messmer, R. P.; Maylotte, D. H. K-edge absorption spectra of selected vanadium compounds. *Phys. Rev. B* **1984**, *30*, 5596−5610.

(36) Giorgetti, M.; Passerini, S.; Smyrl, W. H.; Mukerjee, S.; Yang, X. Q.; McBreen, J. In Situ X-Ray Absorption Spectroscopy Characterization of $V_2O_5$ Xerogel Cathodes upon Lithium Intercalation. *J. Electrochem. Soc.* **1999**, *146*, 2387−2392.

(37) Stizza, S.; Mancini, G.; Benfatto, M.; Natoli, C. R.; Garcia, J.; Bianconi, A. Structure of oriented $V_2O_5$ gel studied by polarized x-ray-absorption spectroscopy at the vanadium K edge. *Phys. Rev. B* **1989**, *40*, 12229−12236.

(38) Mansour, A. N.; Smith, P. H.; Balasubramanian, M.; McBreen, J. In Situ X-Ray Absorption Study of Cycled Ambigel $V_2O_5 \cdot nH_2O$ ($n \approx 0.5$) Composite Cathodes. *J. Electrochem. Soc.* **2005**, *152*, A1312.

(39) Chen, C. L.; Dong, C. L.; Ho, Y. K.; Chang, C. C.; Wei, D. H.; Chan, T. C.; Chen, J. L.; Jang, W. L.; Hsu, C. C.; Kumar, K.; Wu, M. K. Electronic and atomic structures of gasochromic $V_2O_5$ films. *Europhys. Lett.* **2013**, *101*, 17006.

(40) Wei, Y.; Zhou, J.; Zheng, J.; Xu, C. Improved stability of electrochromic devices using Ti-doped $V_2O_5$ film. *Electrochim. Acta* **2015**, *166*, 277−284.

(41) Yu, H.; Rui, X.; Tan, H.; Chen, J.; Huang, X.; Xu, C.; Liu, W.; Yu, D. Y. W.; Hng, H. H.; Hoster, H. E.; Yan, Q. Cu doped $V_2O_5$ flowers as cathode material for high-performance lithium ion batteries. *Nanoscale* **2013**, *5*, 4937−4943.